Journal of The Electrochemical Society, 2022 **169** 030515

State of the Art of Lithium-Ion Pouch Cells in Automotive Applications: Cell Teardown and Characterization

F. J. Günter[1,=,z] **and N. Wassiliadis**[2,=]

[1]*Technical University of Munich, Germany; School of Engineering & Design, Department of Mechanical Engineering; Institute for Machine Tools and Industrial Management, Boltzmannstr. 15, 85748 Garching, Germany*
[2]*Technical University of Munich, Germany; School of Engineering & Design, Department of Mobility Systems Engineering; Institute of Automotive Technology, Boltzmannstr. 15, 85748 Garching, Germany*

A large-format pouch cell with a nominal capacity of 78 Ah from the Volkswagen ID.3 was disassembled and analyzed to characterize the state of the art of industrial-scale cells in automotive applications. The cell components were separated from each other, geometrically measured, and weighed to quantify the volume and weight fractions from electrode to cell level. Material samples from the electrodes were characterized by scanning electron microscopy (SEM), elemental analysis, and mercury porosimetry. Half cells were built post mortem and assessed in electrochemical tests. The results revealed a stacked cell of laminated electrode layers. The cathode showed a bi-modal particle distribution and its active material ranged with $LiNi_{0.65}Mn_{0.2}Co_{0.15}O_2$ in between NMC622 and NMC811. Silicon-free graphite was used as the anode active material. Over 75% of the cell mass and over 81% of the cell volume directly contribute with its active material to the specific energy of 268 Wh kg^{-1} and energy density of 674 Wh L^{-1} at cell level. 91% of the anode and 93% of the cathode were utilized in the pristine cell, respectively. In charge rate tests, the anode was identified as the limiting electrode. The results provide valuable insights into the state of the art of automotive lithium-ion batteries and serve as a reference for scientific research.
 [DOI: 10.1149/1945-7111/ac4e11]

Manuscript submitted October 25, 2021; revised manuscript received December 19, 2021. Published March 9, 2022.

The lithium-ion cell is an instrumental technology for achieving climate goals such as limiting global carbon dioxide emissions. For laying the foundation for a wireless society without fossil fuels based on this technology, Stanley Whittingham, John Goodenough, and Akira Yoshino received the Nobel Prize in 2019.[1] Since lithium-ion cells were commercialized by Sony in 1991, the demand for lithium-ion cells has grown steadily and primarily through their use in portable consumer electronics devices.[2] Meanwhile, the lithium-ion cell has also come to be seen as an enabler for electromobility.[3,4] While many studies have been published at the laboratory to pilot scale[5–7] there is little insight into how commercial cells are manufactured and designed in industry, as there are a vast number of possibilities in material selection,[8,9] cell format,[10–12] and production processes as well as the linking of the processes and their impact on costs and quality.[13–17] Commercial product design, however, gives academic research the opportunity to put its results into an application context. Laboratory-scale research is conducted primarily on coin cells,[18–20] three-electrode cells[21–23] and small-format pouch cells[24,25] to gain fundamental knowledge at the material or electrode level. However, these cells have little in common with industrial high-capacity cells. Low-capacity cells often benefit from an excess of electrolyte, optimal pressure, homogeneous pressure distribution, a highly porous separator, and good heat dissipation in comparison to the upscaled product. In addition, they are hardly affected by gassing due to the high ratio of dead volume to active material (and the highly porous separator). Half-cell results in mAh cm^{-2} or mAh/g_{AM} as well as the advantages already mentioned can lead to unrealistic predictions for industrial applications in Wh kg^{-1}or Wh L^{-1} at the cell level, especially if only a few cycles are measured.

This paper aims to make commercial cell characteristics accessible, not only to provide a realistic and quantified reference for academia but also to increase the understanding of cells as a mass product and the understanding of the transfer from laboratory cells to application. Therefore, an automotive pouch cell extracted from a Volkswagen ID.3 with a nominal capacity of 78 Ah was characterized, disassembled, and analyzed using scanning electron microscopy (SEM), elemental analysis, mercury porosimetry, weighing, geometric and electrochemical measurements. The electrochemical measurements were ascertained for each electrode by building half cells post mortem. Conclusions are drawn for the electrode design and the cell architecture. Based on these, assumptions were made for the production processes used to manufacture the cell. Furthermore, it is shown how the electrodes contribute to the electrochemical performance of the full cell.

Experimental

Battery cell teardown.—The cell shown in Fig. 1a with a rated capacity of 78 Ah was CC-CV discharged with C/4 to 3.0 V and a cutoff current of 1 A to reduce the energy content due to safety reasons. Following the procedure, the cell was introduced into the glove box. For this purpose, the airlock was purged with inert gas (without going lower than 800 mbar). The cell was weighed and placed on a rubber mat to prevent a short-circuit fault. The cell was opened using a scalpel. As shown in Fig. 1b, the cut was made at the outermost edge of the deep-drawn pocket and on three sides along the stack geometry. The metal foils were cut in front of the weld seam on the tab. The stack was removed from the packaging and the adhesive strips were peeled off. Sheet by sheet the separator, cathode, and anode were pulled off the stack as shown in Fig. 1c. For a complete disassembly of the cell, the conductor tabs were cut free from the pouch foil, see Fig. A·2 in the Appendix.

All components were collected, weighed and stored separately according to the categories packaging, tapes, anodes, anode tab, cathode, cathode tab, and separator. The thickness was measured with a Micromar *40 EWRi* (Mahr, Germany). Width and length were measured using calipers and a measuring stick. For the measurements of the separator, anode, and cathode, eight sheets were measured. A punch from Nogami (Japan) with a diameter of 14 mm for the cathode and 15 mm for the anode was used to punch out multiple electrode samples for the half cells, the Mercury porosimetry, the scanning electron microscopy (SEM), the elemental analysis, and the determination of the loading. Four coin electrodes each, for both anode and cathode, were weighed, devarnished to the substrate foil using isopropanol as a solvent under rubbing, and weighed again. The remaining metal foils were then measured for their thicknesses.

[=]Both authors contributed equally.
[z]E-mail: florian.guenter@iwb.tum.de

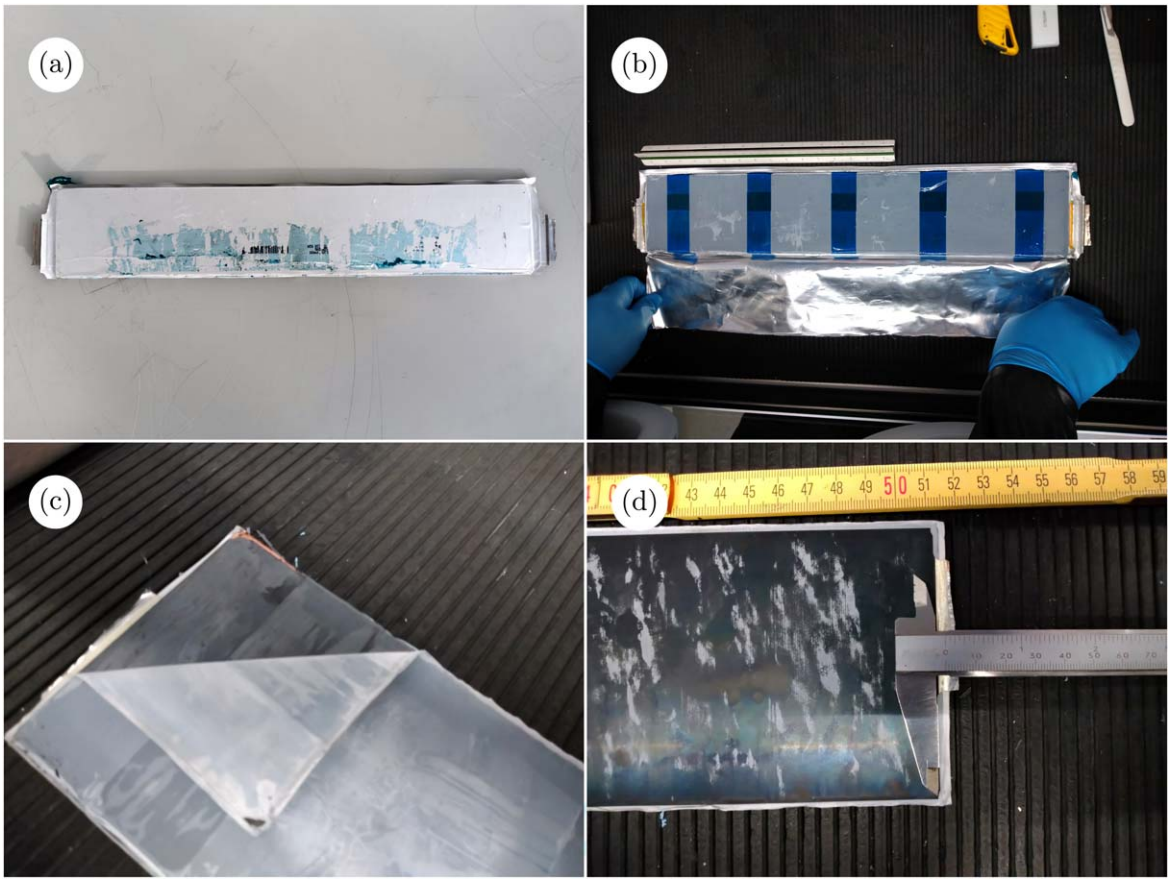

Figure 1. Cell opening procedure and component disassembly within an Argon-filled glove box. (a) Pristine cell extracted from a module, (b) cell stack wrapped with blue assembly tapes within the pouch packaging during opening, (c) separator on top of the anode layer during peel-off, (d) cathode layer on top of the separator sheet.

Microscopy and elemental analysis.—For the SEM, a *JEOL IT-200* (JEOL, Japan) at 15 kV with an LEI detector was used at different magnifications (see images). The same instrument was used for the energy-dispersive X-ray spectroscopy (EDX).

For the elemental analysis, three samples per electrode and measurement were sent to the *Mikroanalytisches Labor Pascher* (Remagen, Germany). There, a determination of carbon, hydrogen, and silicon was conducted on the anodes and a determination of cobalt, lithium, manganese, and nickel was conducted on the cathodes. Samples were combusted at 1200 °C in a purified oxygen stream to detect carbon. The resulting carbon dioxide was absorbed in 0.1 N NaOH and was detected conductometrically. To detect hydrogen, samples were combusted at 1050 °C in an oxygen stream. The water formed on combustion was detected by IR-spectroscopy. The determination of silicon was conducted using an extraction with nitric acid and hydrofluoric acid at 130 °C for over 10 h combined with an inductively coupled plasma atomic emission spectroscopy (ICP-AES). Cobalt, lithium, manganese and nickel were measured by dissolution with nitric acid at 180 °C for over 10 h followed by the ICP-AES measurement. For all ICP-AES measurements, the *iCap 6500* (Thermo Fisher Scientific, U.S.) was used.

Mercury porosimetry.—The electrodes were washed in a mixture of ethylene carbonate (EC) and diethyl carbonate (DC) to reduce the amount of dried electrolyte residues on the surface and in the pores. For this purpose, the electrodes were immersed in a solution with a weight ratio of 1:7 (EC:DC) for 15 min. Afterward, the electrodes were dried at 70 °C for 12 h.

The mercury intrusion/porosity measurements were conducted using a *Belpore LP* and a *Belpore HP* system (Microtrac Retsch GmbH, Germany) at 19 °C. In a glove box, the electrode samples were cut into multiple pieces (1 mm × 4 mm). Each probe consisted of pieces weighing together 0.35 g. The probes were put in a dilatometer each. The dilatometers were degassed for 10 min and filled with 450 mm^3 of mercury in the *Belpore LP* prior to the first measurements. The pressure was increased at a rate of 6 to 19 MPa min^{-1}. After the low-pressure measurements, the dilatometers were inserted into the *Belpore HP* device. The starting pressure was 0.013 MPa. The pressure was increased at a rate of 6 to 19 MPa min^{-1} to a maximum pressure of 400 MPa. (After each measurement, the pressure was decreased at a rate of 8 to 35 MPa min^{-1}.) Based on the SEM images, the upper evaluation limits for the pore diameter were set to 30 μm for the anode and 7 μm for the cathode.

Post mortem half cell setup and formation.—The half cells were built similar to the procedure according to Murray et al.[26] in a *CR2032* casing (Hohsen, Japan) with a lithium chip of 0.23 mm thickness and a diameter of 15.5 mm (Pi-Kem Limited, Great Britain) as the negative electrode.

The sequence for assembly procedure began with the lower housing, in which the positive electrode (anode or cathode sample of the large-format cell) was inserted. Two glass fiber separators (VWR, Germany) with a thickness of 0.25 mm and diameter of 16 mm were mounted on top of the electrode followed by the lithium chip. The set-up was finalized with a 0.5 mm thick spacer with a diameter of 16 mm and a spring. The half cells were closed with the upper casing. After the assembly of the electrode, of each separator and of the lithium chip, 50 μl *LP572* (BASF, Germany) were dosed as electrolyte resulting in a total amount of 200 μl per cell. The

electrolyte consisted of a 1 M solution of $LiPF_6$ in a mixture of ethylene carbonate (EC) and ethyl methyl carbonate (EMC; weight ratio EC:EMC of 3:7) with 2 wt.% vinylene carbonate (VC).

Eight half cells underwent a ∼1 h rest period for wetting. Afterward, they were connected to a *CTS Lab XL* battery cycler (BaSyTec GmbH, Germany). To allow for a post-formation of the solid electrolyte interphase (SEI),[27,28] all half cells were cycled between 10 mV and 1.5 V for the anode and between 2.5 V and 4.2 V for the cathode, as shown by Fig. 2. For (post-)formation, the current rate was set to C/10 to avoid stressing the the half cells, which have a high failure rate if built from commercial cells post mortem.[29] As the individual capacities were unknown, the applied current rate refers to a calculated capacity of the individual stamps. The calculation followed the theoretical estimation of the areal capacity of the pristine cell ($q_{\text{Electrode}}$) based on the rated pristine cell capacity of 78 Ah according to

$$q_{\text{Electrode}} = \underbrace{b \cdot l}_{\text{Electrodesurface}} \cdot \underbrace{18}_{\text{Electrodelayer}} \cdot \underbrace{2}_{\text{Double-coated}} \quad [1]$$

for the individual electrodes, with the electrode width b and length l. The theoretical areal capacity was further used to calculate the absolute half cell capacities Q_{HC} according to

$$Q_{\text{HC}} = A_{\text{HC}} \cdot q_{\text{Electrode}} = \left(\frac{d}{2}\right)^2 \cdot \pi \cdot q_{\text{Electrode}} \quad [2]$$

with the individual stamp diameter d for the anode and cathode, respectively. After three formation cycles, half cells with reproducible voltage traces and coulombic efficiencies above 97% were selected for further investigation of the electrochemical performance.

Test procedures for electrochemical performance assessment.—To assess the electrode capacity utilization of the electrodes, a selected sample of each electrode was subjected to C/50 in constant current (CC) mode, known as the pseudo-open-circuit-voltage (pOCV) technique.[30] Likewise, the procedure was performed with a pristine cell. The measurements were used for balancing and alignment of the half cell OCV to the pristine cell OCV, in accordance with the work of to Honkura and Horiba,[31] who used this method to reveal insights into the characteristic stage transitions of both electrodes. The half cells were discharged from a pristine cell perspective, i.e., delithiating the anode and lithiating the cathode. The voltage window of these tests differed from the formation voltage window: The investigated half cells achieved a stable cycling during formation and were subjected to the larger voltage window as it is used in the pristine cell. Here, the anode was cycled between 1 mV and 1 V, and the cathode was cycled between 2.5 V and 4.3 V. The pristine cell was discharged between 2.5 V and 4.2 V to account for the operating voltage window during operation. Both, half cells and the pristine cells, were subjected to C/50 CC charge sequences for pOCV determination within the respective voltage bounds. The capacity retention of the pristine cell, pOCV, and the geometrical measures were used for energy density calculations at cell level.

To further investigate into the charging capability of the cell, charge rate tests with an increasing rate were performed on the half cells in the charge direction from a full cell perspective. As both half cells slightly age during the rate tests, the C-rate is referred for an initial capacity check prior to the rate tests. Both electrodes were initially lithiated/delithiated to the respective voltage bound and subsequently delithiated/lithiated with C/10 in CC mode to determine the actual capacity of the half cells. During this procedure, the anode was cycled between 1 mV and 0.5 V, as the steep potential increase beyond 0.5 V did not contribute essentially to the overall charge throughput.

All aforementioned tests were performed at 20 °C in a thermal chamber starting from a thermally relaxed state (>4 h relaxation).

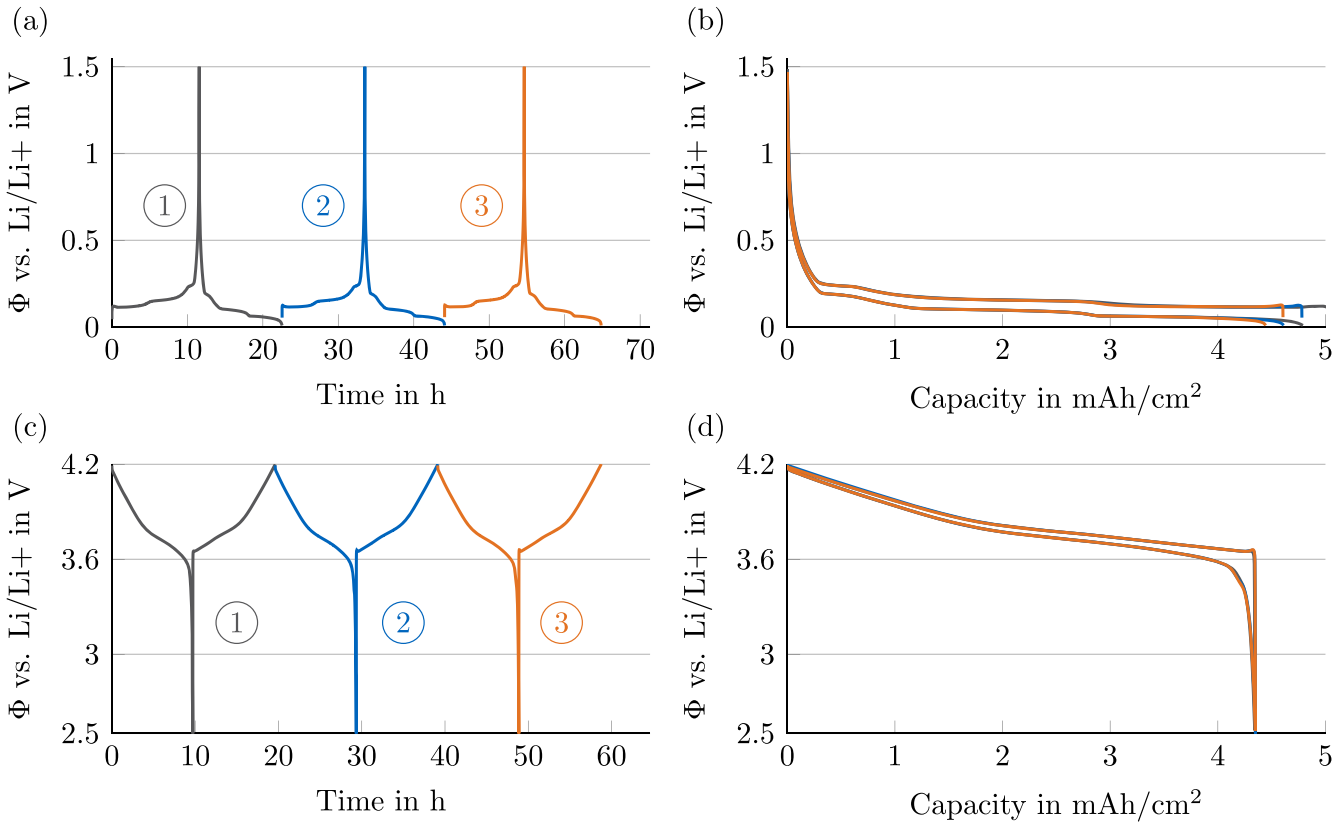

Figure 2. Post-teardown formation cycles with voltage over time in (a)/(c) and voltage over capacity in (b)/(d) for anode and cathode half cells, respectively. Colored curves represent the three consecutive charge/discharge cycles.

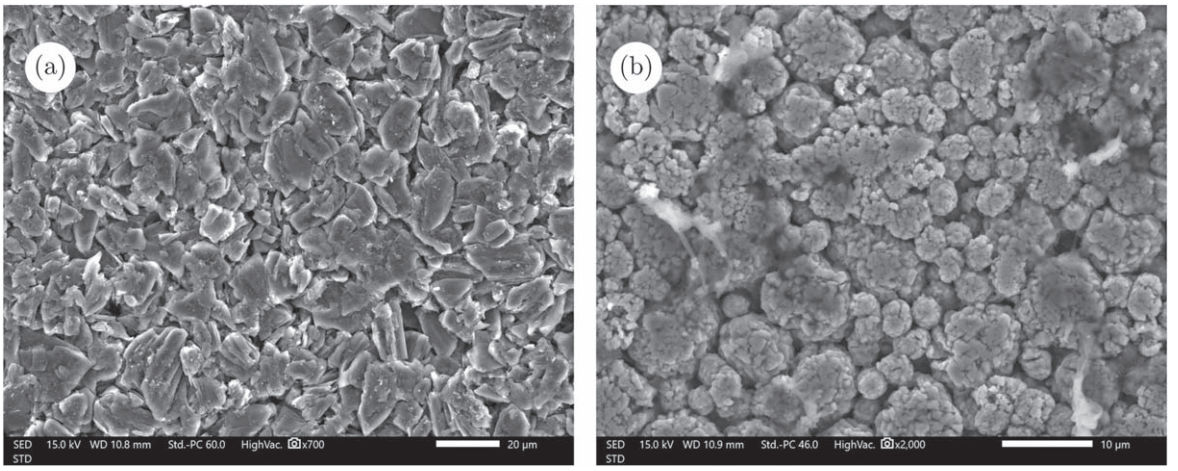

Figure 3. SEM images of (a) the anode and (b) the cathode.

Results and Discussion

Electrode design.—Figure 3 shows the SEM images of the anode (a) and the cathode (b). The anode consists mainly of flake-shaped particles up to a diameter of 20 μm. The image of the cathode shows a bimodal distribution with spherical particles of approx. 3 μm and 9.5 μm diameter. These secondary particles are composed of densely packed primary particles ($\leqslant 1$ μm). The four largest mass fractions of the anode coating were given by the EDX measurements with 86.4 w% for carbon, 6.4 w% for oxygen, 5.7 w% for fluorine, and

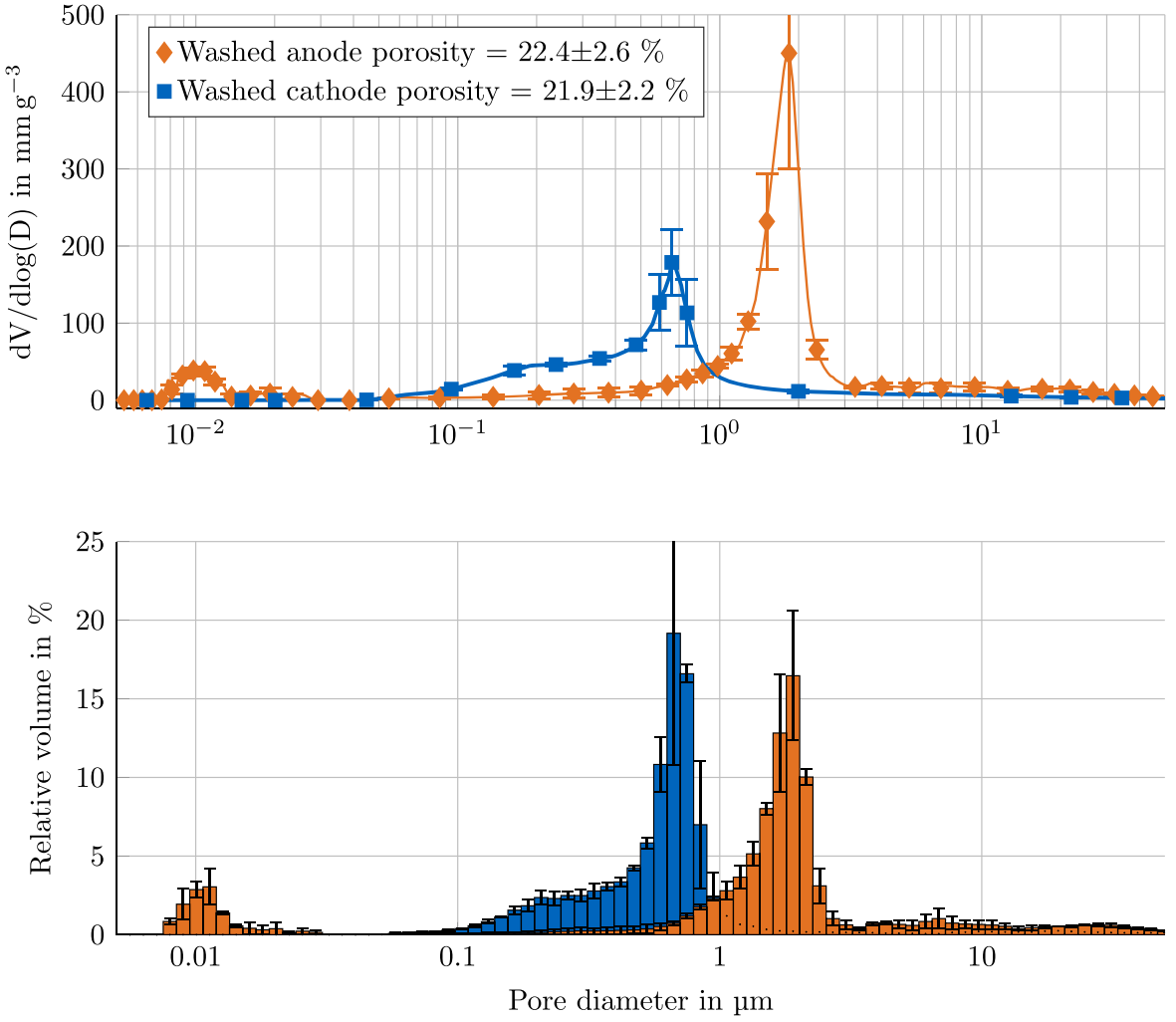

Figure 4. Mercury porosimetry measurements of the washed anode and cathode (top). Share of the pore volume according to the pore size (bottom). The pore diameter was divided into 20 steps (bars) per decade. For both electrodes a total porosity of approx. 22% was measured, which is attributed to dried electrolyte residues in the pores as the porosity of the electrodes prior to filling is assumed to be higher.

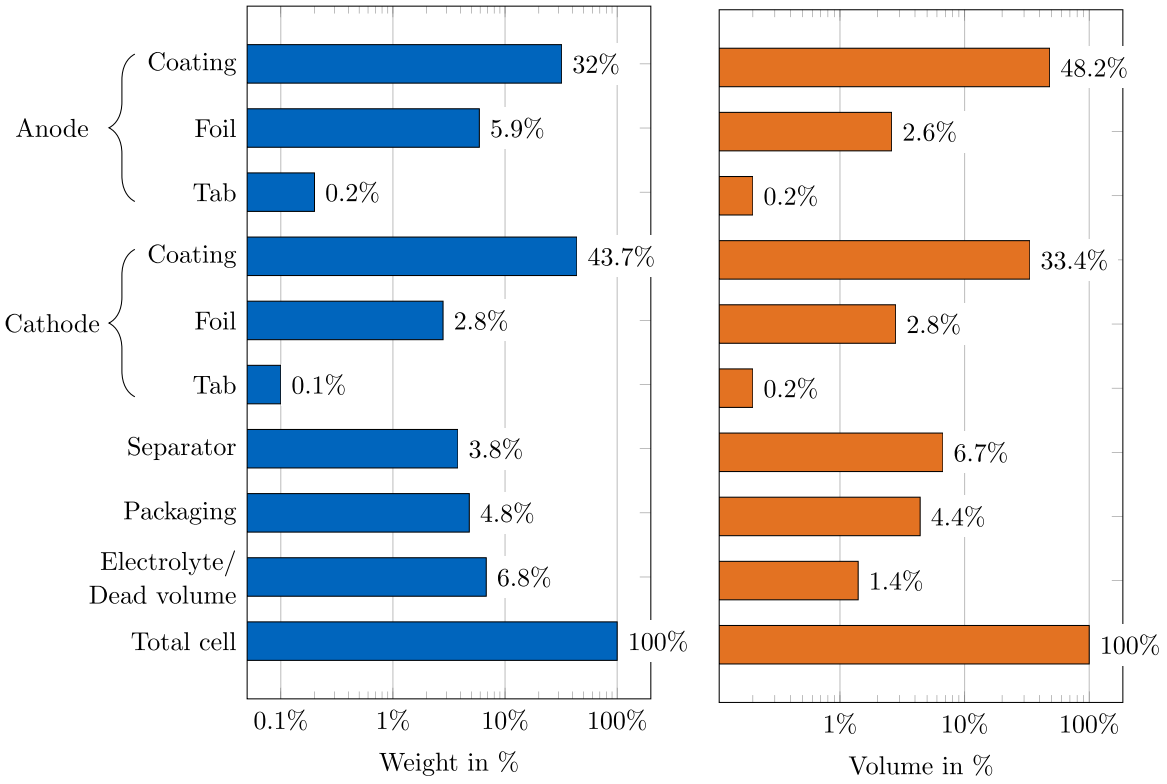

Figure 5. Measured weight and volume shares of each component as part of the total cell weight and volume, respectively. The packaging includes the tapes. The electrolyte describes the difference between the cell weight and the total weight of individual components after disassembly and is attributed to the evaporated solvents. The dead volume was calculated from the difference between the individual volumes and the volume of the outer cell dimensions. The compression of the cell, as well as laminate residues, were taken into account in the calculations using the minimum values of the coating thickness of the electrodes and the minimum measurement of the separator thickness.

1.1 w% for phosphorus. The laboratory elemental analysis confirmed the results of the EDX measurements with a carbon content of 87% and a hydrogen content of 0.9%. The high carbon content as well as the typical shape of the particles is proof for graphite as active material in the anodes. Interestingly, neither the EDX nor the ICP-AES showed any signs ($\geqslant$0.05 w%) of silicon in the anode. The high percentage of oxygen in the layer is an indication of SEI, as well as solvent residues from the electrolyte in the electrode. Hydrogen and phosphorus are components attributable to the electrolyte[32] and SEI,[28] but also to the binder. For the cathode, the EDX showed a NMC as the active material with a composition between NMC622 and NMC811. Only evaluating the elements nickel, manganese and cobalt, the weight shares resulted in 65.1 w% for nickel, 15.5 w% for cobalt, and 19.4 w% for manganese. The ICP-AES included the lithium content, which was measured to 5.99 ± 0.05 w%. Nickel had the highest share with 33.53 ± 0.32 w%. Furthermore, the cobalt content was with 7.78 ± 0.08 w% lower than the manganese content of 9.45 ± 0.1 w%. In combination with the molar mass of the metals the cathode material was determined to $LiNi_{0.65}Mn_{0.2}Co_{0.15}O_2$.

The electrodes were coated on both sides. The footprint of the anode coating is $9.7 \times 51.2\,cm^2$ and of the cathode coating $9.5 \times 51\,cm^2$. The tabs are positioned oppositely at the end of the long electrode dimension. Therefore, three possibilities for the electrode production arise: The first possibility consists of an intermittent coating process with a resulting pattern every 51.2 (+0.8) cm for the anode and every 51(+0.8) cm for the cathode followed by a slitting process. The slitter allows the parallel production of multiple electrodes on one coater as it cuts mechanically or using a laser in the direction of the material flow.[17] The second possibility is a continuous coating process with a coating width according to the electrode length. Coating twice the electrode width continuously in combination with a slitting in the middle of the coating is the third variation. As the first possibility promises the highest throughput (and the second the lowest) it is the most likely variant for cost reasons. Regardless of the variation, the electrodes were coated on both sides with a 12 μm copper foil used for the anode and a 14 μm aluminum foil for the cathode. Both, a parallel realization with subsequent drying or a sequential process with intermediate drying are possible.[16] The former process is superior in regard to throughput and energy consumption. The anode coating has a (single-sided) thickness of 115.3 μm at a loading density of 18.1 mg cm^{-2}. The single-sided cathode coating is 87.3 μm thick and has a loading of 27.9 mg cm^{-2}. Changes after electrode production should be considered regarding the weight and the pores of the coating. The pores of the electrodes were filled with electrolyte liquid.[33] During the disassembly of the cell, the electrolyte solvents with a low boiling point evaporated leaving conducting salt and solvent with a high boiling point behind. Furthermore, passivation layers like the SEI were built during formation.[27] Both increase the weight and decrease the porosity of the electrodes in comparison to the pristine state after electrode production. In this context, Fig. 4 shows the result of the Mercury intrusion after washing the electrodes to reduce the electrolyte residues. The anode shows two normal distributions with peaks at approx. 10^{-2} μm and 2 μm pore diameter. The distribution of pore volume with regard to pore size is wider for the cathode. It has a peak at approx. 0.7 μm and expands to lower pores down to 0.1 μm unilaterally. The asymmetric pore size distribution of the cathode is assumed to result from the bimodal particle distribution. According to Schreiner et al.,[6] pore diameters below 0.24 μm represent the space inside secondary particles or carbon black for cathodes. Pore diameters up to 16 μm represent the space between secondary particles and even greater pore diameters are attributed to surface roughness.[6] Hence, the cathode has neither measurable pores in the secondary particles nor carbon black. The anode pores, however, include conducting agents. Furthermore, the high pore volume fraction of small pore

diameters is a clear indication for calendering of the electrodes during manufacturing.[6]

Cell architecture.—The cell stack was wrapped with five tapes and positioned in the deep-drawn pocket of the pouch bag. The position was fixed on the left and the right side with the tabs in the seal seam. The stack consisted of single sheets beginning with a separator followed by an anode, a separator, and a cathode in repeating order. The sequence ended on the other side again with an anode and finally with a separator. In total, the stack consisted of 38 separator sheets, 19 anode sheets, and 18 cathode sheets.

Anodes and cathodes show both white residues on only one side of the sheet and had different resistance to the manual separation of separator and electrode sheet. The SEM images (Fig. A·1) showed shred-like residues adhering to one side of each electrode. Hence, it is very probable that the electrodes were cut to the footprint plus the tab connection via laser or mechanically[11] and the single sheets were laminated to the separator. It is assumed that the lamination was a continuous process according to Ref. 34 and the electrode-separator compartments were cut afterward to simplify handling: The separator on its own is inherently unstable as it has a thickness of 17.6 μm at a footprint of $10 \times 51.7\,cm^2$. Furthermore, the lamination halves the number of sheets to stack in the subsequent stacking process. The comparison of electrode footprints shows that a positioning accuracy of ±1 mm is necessary during stacking so that the cathode coating area is always covered by the anode. A subsequent lamination of the stack by increased temperature and pressure in order to fix the position of the sheets is possible. However, no evidence was found for this.

As conductor tabs, aluminum and nickel-plated copper was used. Both current conducting cross-sections of the tabs resulted in $22.5\,mm^2$. The conductor tabs have different patterns embossed on the front compared to the back (Fig. A·2). Such patterns are embossed by means of ultrasonic welding in the metal[35] in contrast to laser welding.[36] Due to the two different patterns, it was welded in two steps. First, the tapered end Sections of the substrate foils (with a cross-sectional area of $0.54\,mm^2$ per anode and $0.64\,mm^2$ per cathode) were welded together. Then they were welded on the tabs. Probably then, the electrode-separator stack was inserted into a deep-drawn aluminum composite foil, which was sealed on two sides (left and right at the tabs) as the seal seams indicate.

The cell format of stack and flexible pouch foil allows electrolyte dosing in one step as well as faster wetting than with wound electrode-separator assemblies.[37] Therefore, it is assumed that the electrolyte was dosed under evacuation in one step and the cell was sealed subsequently, which resulted in a closed wetting. As reported in the literature,[6] a degassing step was probably implemented after or during the formation[38,39] removing the gas bag by cutting and sealing the cell to its final format. The cell weighs 1.101 kg and has a volume of 0.438 L. Figure 5 shows the proportions of the weight and volume of the cell of each of the components. The coatings of the electrodes containing the active material account for 75.7 w% and 81.6 v% of the cell. Furthermore, the dead volume with approx. 1.4% shows the high degree of space utilization, as pouch cells are advantageous in terms of energy and packing density.[12]

As already mentioned for the porosimetry, dried electrolyte residues in the pores of the electrodes have an impact on the weight. Here, the residues lead to higher weights and, thus, higher weight fractions of the coatings compared to the pristine state of the electrodes before filling and wetting with electrolyte liquid. This too high electrode content actually belongs to the electrolyte, which has a significant influence on the weight of the cell.[40] Furthermore, the thickness of the cell was higher than the sum of the mean thicknesses after assembly. Therefore, the compression of the components due to pressure difference between inside of the cell and the environment is assumed. Another possibility is an increase in the thickness of the electrodes due to laminate residues on the surface or plastic deformation during the manual peel-off. To account for these effects, the minimum value of electrode, as well as separator thickness, was used for the volume calculation, and not the mean. For details on the absolute values, see Tables A·I, A·II, and A·III.

Nevertheless, the influence of upscaling and cell format becomes particularly clear comparing the values with the weight and volume fractions of the half cells. In the anode/cathode of the post mortem half cells, the casing contributed 90.7/90.6 w% and 49.3 v%. The active material (including the lithium chip plus the respective electrode coating) accounted only for 1.8/2.1 w% and 6.4/5.7 v%. Compared to the automotive cell, no electrolyte residues are on the separator and additional electrolyte was added, but the resulting electrolyte only amounted to a share of 7.8/7.7 w%. The empty space of the coin cells is with 34.5/35.1 v% in relation to the automotive cell significantly higher and, e.g., allows for the storage of excess electrolyte, which is not wetting the pores.

Electrochemical performance.—The measured anode potentials Φ capture the staging behavior as expected for the lithiation processes of graphite.[41,42] Three distinct voltage plateaus as reported by Nitta et al.[43] are shown in Fig. 6a. At ∼100 mV, phase transitions from LiC_6 to LiC_{12} occur keeping the potential almost constant. With further delithiation, an additional plateau evolves at ∼140 mV, where LiC_{12} and LiC_{24} coexist. At ∼230 mV, the last phase transition occurs followed by a steep potential increase to the last stage of delithiated graphite C_6. Also, the measured cathode potential shows characteristic features in the measured potential,[44] as illustrated in Fig. 6b. A steep voltage decrease is observable close to the fully lithiated cathode. Also, the voltage gradient changes at ∼3.7 V. In total, a charge throughput of $5.23\,mAh\,cm^{-2}$ and $5.02\,mAh\,cm^{-2}$ was measured during the procedure for the anode and cathode, respectively. Using the charge throughput of both electrodes, the N/P ratio was calculated as 1.04. This is rather low compared to reported design strategies in the literature,[45] leading to an enhanced usable capacity of the cell due to lowered potentials and better anode capacity utilization but also to an increased risk for fast capacity fade during operation as larger anode capacity windows are used during cycling.[46]

The observed clear feature distinctions of both electrodes were subsequently used for determining the electrode utilization and balancing at cell level. The procedure is similar to previous studies[31] and follows a theoretical scaling of both electrode capacities and a horizontal shifting to match the measured full cell potential following

$$U_{OCV} = \Phi^+(Q^+) - \Phi^-(Q^-) = \Phi^+\left(\frac{Q + \sigma_b^+}{S_b^+}\right) - \Phi^-\left(\frac{Q + \sigma_b^-}{S_b^-}\right) \quad [3]$$

with the horizontal alignment coefficient $\sigma_b^{\pm}$ and the scaling factor $S_b^{\pm}$ for each individual electrode. The result of the balancing and alignment of both electrode potentials to the full cell potential is illustrated in Fig. 6c. Within the full cell, 91.8% of the anode capacity is utilized, while 93.7% of the cathode capacity is utilized. The total fitting procedure of the superimposed potentials to the measured potential yields $R2 = 99.97\%$ and a precise match to the distinctive features of the electrode, as visible in Fig. 6d, ensuring the resilience of the determined capacities and capacity ratios.

The pristine cell achieved a C/50 discharge capacity of 79.9 Ah and an energy retention of 295.4 Wh at 20 °C. Taking into account the geometrical and weight measurements from Table A·III, a specific energy of $268\,Wh\,kg^{-1}$ and an energy density of $674\,Wh\,L^{-1}$ was determined at cell level. For comparison, the cathode post mortem half cells reached only $8.25\,Wh\,kg^{-1}$ and $24.42\,Wh\,L^{-1}$ under same conditions due to the lower active material share of the coin cells. Using graphite/NMC622, larger hard case cells with a capacity of 22.01 Ah at C/5 showed with $138.26\,Wh\,kg^{-1}$ and $293.08\,Wh\,L^{-1}$ lower properties as well.[47] Even the use of pouch cells on laboratory scale (based on graphite/NMC532 with 0.24 Ah at C/20) just achieved $200\,Wh\,kg^{-1}$ and $390\,Wh\,L^{-1}$.[5] Thus, the measured characteristic values of the automotive cell show the great influence of the cell architecture and the upscaling to high capacities.

In a subsequent charging current rate test, illustrated in Fig. 7, the capacity retention under increasing charging currents of the half cells

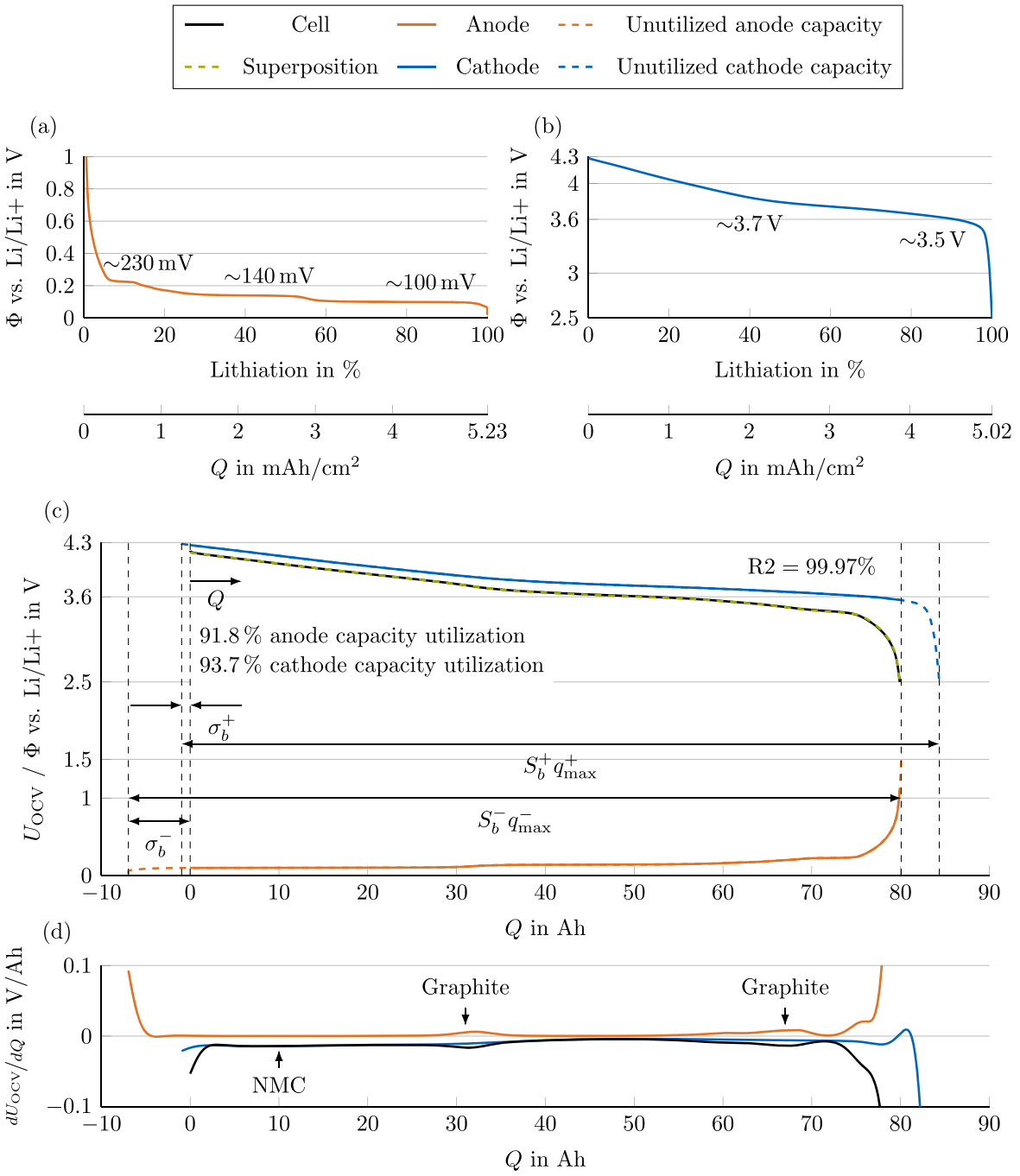

Figure 6. Open-circuit potentials Φ vs Li/Li+ of (a) anode and (b) cathode, determined by C/50 discharge from a full cell perspective, i.e., C/50 delithiation/charge of the anode/anode half cell and C/50 lithiation/discharge of the cathode/cathode half cell, respectively. (c) Aligned and balanced half cell potentials to the full cell open-circuit potential determined by a C/50 discharge with quantified capacities and charge utilization of both electrodes. (d) Differential voltage analysis of the individual open-circuit potentials.

is measured. It should be noted that the results only serve as a qualitative reference, as the electrolyte system of the pristine cell has been changed due to the addition of *LP572* (BASF, Germany) to the original unknown electrolyte composition. Consequently, a mixture with possible residuals of the original electrolyte system during the post mortem half cell setup procedure is highly probable. This may change the half cell electrochemical performance compared to the pristine cell. The overpotentials in the electrolyte are expected to exceed the overpotentials in the pristine electrolyte system of the full cell prior to disassembly. Furthermore, the lithium counter electrode interferes and also lead to additional unintended overpotentials. It should be noted, that C-Rates are therefore not directly comparable to the pristine cell. However, the capacity retention of both half cells in the performed test is comparable, as both half cells are build in the same way and suffer under similar artificial overpotentials.

While the NMC cathode achieves a rather stable capacity retention up to 1C, the anode capacity decreases two-fold at a rather low rate of C/2. At a current rate of 1C, the anode charge throughput is minimized and negative potentials are reached early. Based on the aforementioned observations, it is mainly the anode that limits the charging capability of the cell. As a consequence, negative anode potentials are reached during aggressive fast charging of the full cell,

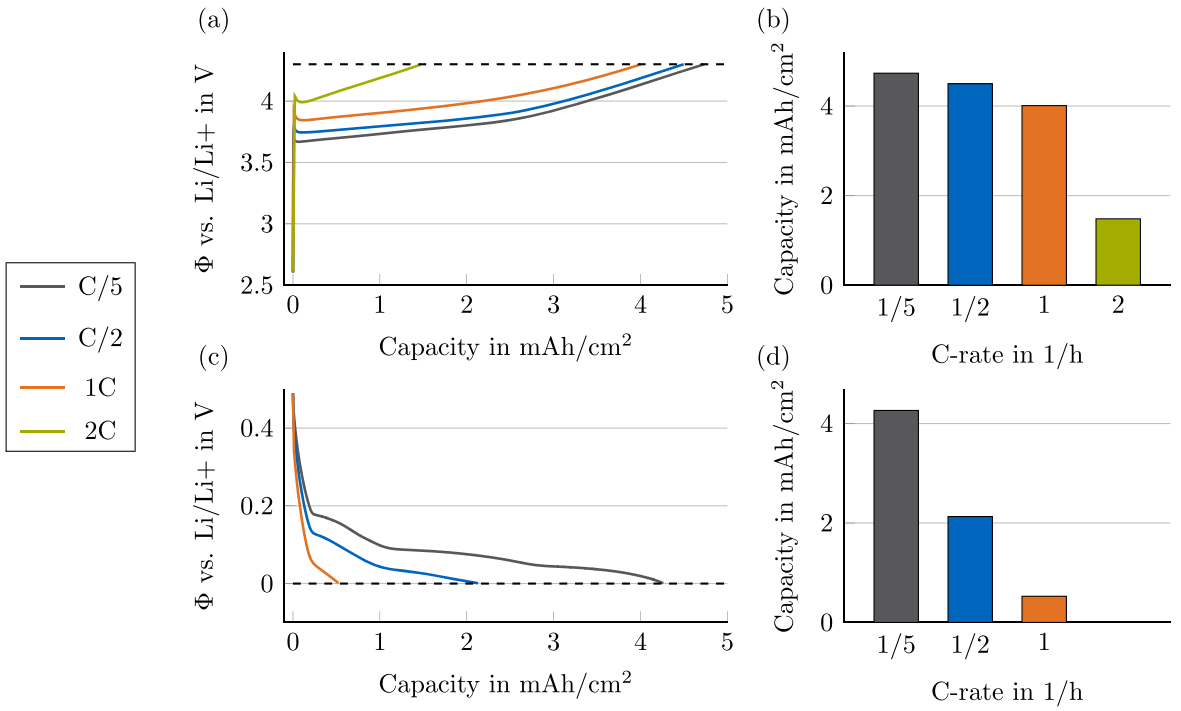

Figure 7. Current rate test of anode and cathode half cells at 20 °C in charge direction from a full-cell perspective. (a)/(b) The evolution of cell potentials Φ vs Li/Li+ with increasing rates and (c)/(d) the corresponding charge throughput until the cutoff voltage limit is reached for cathode and anode, respectively.

increasing the likelihood of lithium deposition.[48] Improvements to the anode charge capability may improve the overall fast charge capability of the cell.

The highest current densities in the cell are in the tapered end Section of the copper foil in front of the tab weld at the anode side. Here, due to the cross-section and the capacity of 79.9 Ah, the current density amounts to 8.22 mm^{-2} in the copper for 1C. At the cathode, the aluminum is exposed to 7.05 mm^{-2} at the same C-rate. The tabs just conduct 3.55 mm^{-2} at 1C.

Conclusions

The aim of this work is to serve as a reference for the state of the art of lithium-ion batteries for industry and academia. Therefore, an industry-scale automotive pouch cell from the Volkswagen ID.3 was subjected to a teardown procedure and its electrode design, cell architecture, and cell performance were analyzed.

A high specific energy of 286 Wh kg^{-1} and a high energy density of 674 Wh L^{-1} was measured by testing the pristine cell prior to disassembly. A thorough mass and volume determination at electrode and cell level attributed these high characteristics to the cell architecture and electrode design: Over 75% of the cell mass and over 81% of the cell volume contributed to the energy content. SEM, EDX, and ICP-AES results revealed a $LiNi_{0.65}Mn_{0.2}Co_{0.15}O_2$ cathode with bi-modal particle size distribution and a silicon-free graphite anode. Building half cells post mortem, it was shown that 91% of the anode capacity and 93% of the cathode capacity participate in the pristine cell. Furthermore, charge capability tests confirmed the anode as the limiting electrode during fast charging.

Acknowledgments

The authors thank Celestine Singer for her support in the SEM measurements and Hans-Christoph Töpper for his support in the porosimetry measurements. Moreover, the authors are grateful to the German Federal Ministry of Education and Research (BMBF) for funding their research within the projects “ExZellTUMIII” (grant number 03XP0255) and “BAld” (grant number 03XP0320B).

CRediT Author Statement

F. J. Günter: Conceptualization, Methodology, Investigation, Writing—Original Draft, Visualization, Resources; **N. Wassiliadis**: Conceptualization, Methodology, Investigation, Writing—Original Draft, Visualization, Resources.

Appendix A

Table A·I. Specifications of the electrodes measured. The thickness of the components refers to the uncompressed state after disassembly. The areal capacity values correspond to a rate of C/50 at 20 °C, as illustrated in Fig. 6.

Property	Anode	Cathode
Foil thickness in μm	12 (Cu)	14 (Al)
Electrode thickness (double-sided) in μm	242.6 ± 6.1	188.5 ± 7.1
Loading Density (single-sided) in mg cm^{-2}	18.1 ± 0.1	27.9 ± 0.1
Areal Capacity in mAh cm^{-2}	5.23	5.02
Footprint of coated area in cm^2	9.7 × 51.2	9.5 × 51
Layers/Number of sheets	19	18
Tab footprint in cm^2	4.5 × 4	4.5 × 4
Tab cross-section cm^2	22.5 (Cu/Ni)	22.5 (Al)

Table A·II. Measured specifications of the separators, tapes, and the pouch foil. The thickness of the components refers to the uncompressed state after disassembly. The footprint of the tapes refers to the unwrapped state. The footprint of the pouch foil refers to the top view of the casing/cell without tabs (and without information about the deep-drawn pocket).

Property	Separator	Tape	Pouch foil
Thickness in μm	17.6 ± 2.1	38	144
Footprint in cm^{-2}	10×51.7	23×3	98×53.5
Number of sheets/stripes/layers	38	5	2

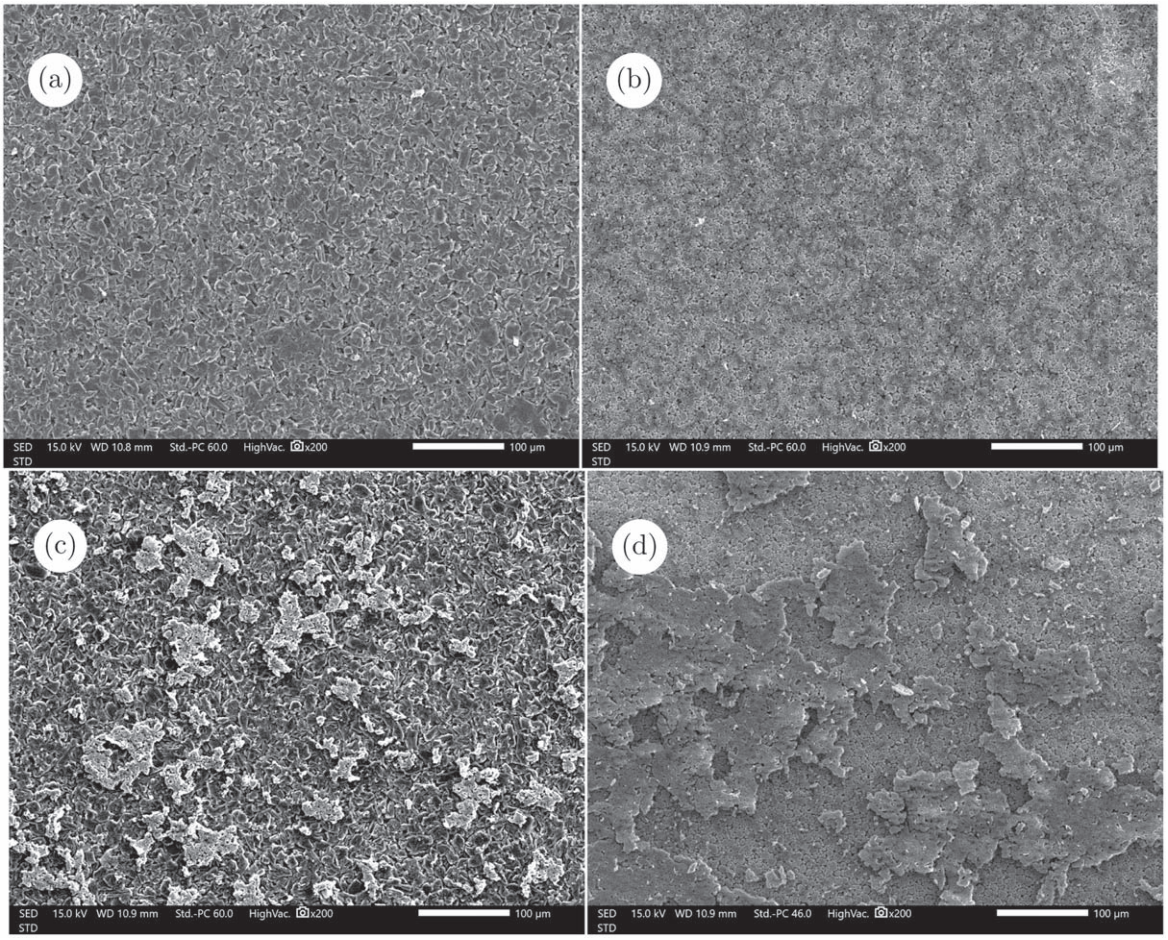

Figure A·1. SEM images of both electrodes from front and back. (a) Anode, (b) cathode, (c) anode with laminate residues and, (d) cathode with laminate residues.

Figure A·2. Embossing on tabs and substrate foil of (a) anode and (b) cathode.

Table A·III. Volumetric and gravimetric proportions of the cell components. The compression of the cell, as well as laminate residues, were taken into account using the minimum measurements of the thickness of the anode (236 μm), the cathode (182 μm), and the separator (15 μm) for the calculation of volume and volume shares of these components. The coatings were calculated from the difference between electrodes and substrate films. The evaporated electrolyte solvent and the empty space were determined from the difference of the cell values and the sum of the individual components. Mean values and standard deviations were determined from measurements of several (4 to 8) samples.

Component	Weight in g	Percentage by weight in %	Volume in cm^3	Volume fraction in %
Cell	1101.4	100	438.3	100
Packaging	50.9	4.6	17.9	4.1
Tapes	1.7	0.2	1.3	0.3
Anode (coated foil)	416.8 ± 12.8	37.8	222.7	50.8
Anode coating	352.2	32	211.4	48.2
Anode foil	64.6 ± 2	5.9	11.3 ± 0.8	2.6
Anode tab	2.3	0.2	1	0.2
Cathode (coated foil)	511.9 ± 23.8	46.5	158.7	36.2
Cathode coating	481.4	43.7	146.3	33.4
Cathode foil	30.5 ± 0.5	2.8	12.4 ± 0.4	2.8
Cathode tab	1.4	0.1	1	0.2
Separator	41.3	3.8	29.5	6.7
Electrolyte evap.	75.1	6.8	—	—
Empty space	—	—	6.3	1.4

ORCID

F. J. Günter https://orcid.org/0000-0002-5967-6801
N. Wassiliadis https://orcid.org/0000-0002-3986-5752

References

1. Press release: The nobel prize in chemistry 2019: They created a rechargeable world (2019) https://www.nobelprize.org/prizes/chemistry/2019/press-release/.
2. A. Yoshino, *Angewandte Chemie (International ed. in English)*, **51**, 5798 (2012).
3. O. Gröger, H. A. Gasteiger, and J. P. Suchsland, "Suchsland, Review-electromobility: Batteries or fuel cells?" *J. Electrochem. Soc.*, **162**, A2605 (2015).
4. D. Andre, S. J. Kim, P. Lamp, S. F. Lux, F. Maglia, O. Paschos, and B. Stiaszny, "Future generations of cathode materials: An automotive industry perspective." *Journal of Materials Chemistry A*, **3**, 6709 (2015).
5. J. E. Harlow et al., "A wide range of testing results on an excellent lithium-ion cell chemistry to be used as benchmarks for new battery technologies." *J. Electrochem. Soc.*, **166**, A3031 (2019).
6. D. Schreiner et al., "Comparative evaluation of lmr-ncm and nca cathode active materials in multilayer lithium-ion pouch cells: Part i. production, electrode characterization, and formation." *J. Electrochem. Soc.*, **168**, 030507 (2021).
7. L. Kraft, T. Zünd, D. Schreiner, R. Wilhelm, F. J. Günter, G. Reinhart, H. A. Gasteiger, and A. Jossen, "Comparative evaluation of lmr-ncm and nca cathode active materials in multilayer lithium-ion pouch cells: Part ii. rate capability, long-term stability, and thermal behavior." *J. Electrochem. Soc.*, **168**, 020537 (2021).

8. M. Winter and R. J. Brodd, "What are batteries, fuel cells, and supercapacitors?" *Chem. Rev.*, **104**, 4245 (2004).
9. H. Li, M. Cormier, N. Zhang, J. Inglis, J. Li, and J. R. Dahn, "Is cobalt needed in ni-rich positive electrode materials for lithium ion batteries?" *J. Electrochem. Soc.*, **166**, A429 (2019).
10. F.-A. Batterien (ed.) 2017 *Entwicklungsperspektiven für Zellformate von Lithium-Ionen-Batterien in der Elektromobilität* http://publica.fraunhofer.de/documents/N-477577.html.
11. J. Kurfer, M. Westermeier, C. Tammer, and G. Reinhart, "Production of large-area lithium-ion cells preconditioning, cell stacking and quality assurance." *CIRP Annals*, **61**, 1 (2012).
12. R. Schröder, M. Aydemir, and G. Seliger, "Comparatively assessing different shapes of lithium-ion battery cells." *Procedia Manufacturing*, **8**, 104 (2017).
13. G. Reinhart, T. Zeilinger, J. Kurfer, M. Westermeier, C. Thiemann, M. Glonegger, M. Wunderer, C. Tammer, M. Schweier, and M. Heinz, "Research and demonstration center for the production of large-area lithium-ion cells Future trends in production engineering." *Future trends in production engineering*, ed. G. Schuh (Springer, Berlin) 3 (2013).
14. D. L. Wood, J. Li, and C. Daniel, "Prospects for reducing the processing cost of lithium ion batteries." *Journal of Power Sources*, **275**, 234 (2015).
15. T. Günther, N. Billot, J. Schuster, J. Schnell, F. B. Spingler, and H. A. Gasteiger, "The manufacturing of electrodes: Key process for the future success of lithium-ion batteries." *Advanced Materials Research*, **1140**, 304 (2016).
16. A. Kwade, W. Haselrieder, R. Leithoff, A. Modlinger, F. Dietrich, and K. Droeder, "Current status and challenges for automotive battery production technologies." *Nat. Energy*, **3**, 290 (2018).
17. Y. Liu, R. Zhang, J. Wang, and Y. Wang, "Current and future lithium-ion battery manufacturing." *iScience*, **24**, 102332 (2021).
18. T. Marks, S. Trussler, A. J. Smith, D. Xiong, and J. R. Dahn, "A guide to li-ion coin-cell electrode making for academic researchers." *J. Electrochem. Soc.*, **158**, A51 (2011).
19. V. Murray, D. S. Hall, and J. R. Dahn, "A guide to full coin cell making for academic researchers." *J. Electrochem. Soc.*, **166**, A329 (2019).
20. N. Ogihara, S. Kawauchi, C. Okuda, Y. Itou, Y. Takeuchi, and Y. Ukyo, "Theoretical and experimental analysis of porous electrodes for lithium-ion batteries by electrochemical impedance spectroscopy 432 using a symmetric cell." *J. Electrochem. Soc.*, **159**, A1034 (2012).
21. S. Solchenbach, D. Pritzl, E. J. Y. Kong, J. Landesfeind, and H. A. Gasteiger, "A gold micro-reference electrode for impedance and potential measurements in lithium ion batteries." *J. Electrochem. Soc.*, **163**, A2265 (2016).
22. J. Landesfeind, D. Pritzl, and H. A. Gasteiger, "An analysis protocol for three-electrode li-ion battery impedance spectra: Part i. analysis of a high-voltage positive electrode." *J. Electrochem. Soc.*, **164**, A1773 (2017).
23. D. Pritzl, J. Landesfeind, S. Solchenbach, and H. A. Gasteiger, "An analysis protocol for three-electrode li-ion battery impedance spectra: Part ii. analysis of a graphite anode cycled vs. lnmo." *J. Electrochem. Soc.*, **165**, A2145 (2018).
24. S. J. An, J. Li, D. Mohanty, C. Daniel, B. J. Polzin, J. R. Croy, S. E. Trask, and D. L. Wood, "Correlation of electrolyte volume and electrochemical performance in lithium-ion pouch cells with graphite anodes and nmc532 cathodes." *J. Electrochem. Soc.*, **164**, A1195 (2017).
25. C. P. Aiken, J. E. Harlow, R. Tingley, T. Hynes, E. R. Logan, S. L. Glazier, A. S. Keefe, and J. R. Dahn, "Accelerated failure in li[ni 0.5 mn 0.3 co 0.2]o 2/graphite pouch cells due to low lipf 6 concentration and extended time at high voltage." *J. Electrochem. Soc.*, **167**, 130541 (2020).
26. V. Murray, D. S. Hall, and J. R. Dahn, "A Guide to Full Coin Cell Making for Academic Researchers." *J. Electrochem. Soc.*, **166**, A329 (2019).
27. E. Peled, "The electrochemical behavior of alkali and alkaline earth metals in nonaqueous battery systems-the solid electrolyte interphase model." *J. Electrochem. Soc.*, **126**, 2047 (1979).
28. S. J. An, J. Li, C. Daniel, D. Mohanty, S. Nagpure, and D. L. Wood, "The state of understanding of the lithium-ion-battery graphite solid electrolyte interphase (sei) and its relationship to formation cycling." *Carbon*, **105**, 52 (2016).
29. J. Sieg, J. Bandlow, T. Mitsch, D. Dragicevic, T. Materna, B. Spier, H. Witzenhausen, M. Ecker, and D. U. Sauer, "Fast charging of an electric vehicle lithium-ion battery at the limit of the lithium deposition process." *Journal of Power Sources*, **427**, 260 (2019).
30. A. Barai, K. Uddin, M. Dubarry, L. Somerville, A. McGordon, P. Jennings, and I. Bloom, "A comparison of methodologies for the non-invasive characterisation of commercial Li-ion cells." *Progress in Energy and Combustion Science*, **72**, 1 (2019).
31. K. Honkura and T. Horiba, "Study of the deterioration mechanism of LiCoO2/graphite cells in charge/discharge cycles using the discharge curve analysis." *Journal of Power Sources*, **264**, 140 (2014).
32. K. Xu, "Electrolytes and interphases in li-ion batteries and beyond." *Chem. Rev.*, **114**, 11503 (2014).
33. T. Knoche and G. Reinhart, "Electrolyte filling of large-scale lithium-ion batteries: Main in uences and challenges for production technology." *Applied Mechanics and Materials*, **794**, 11 (2015).
34. M. Frankenberger, M. Singh, A. Dinter, S. Jankowksy, A. Schmidt, and K. H. Pettinger, "Laminated lithium ion batteries with improved fast charging capability." *Journal of Electroanalytical Chemistry*, **837**, 151 (2019).
35. S. Shin, S. Nam, J. Yu, J. Park, and D. Kim, "Ultrasonic metal welding of multilayered copper foils to nickel-plated copper sheet in lithium-ion battery cell." *Metals*, **11**, 1195 (2021).
36. S. Grabmann, J. Kriegler, F. Harst, F. J. Günter, and M. F. Zaeh, "Laser welding of current collector foil stacks in battery production-mechanical properties of joints welded with a green high-power disk laser." *The International Journal of Advanced Manufacturing Technology*, **118**, 2571 (2021).
37. F. J. Günter, S. Rössler, M. Schulz, W. Braunwarth, R. Gilles, and G. Reinhart, "Influence of the cell format on the electrolyte filling process of lithium-ion." *Energy Technology*, **3**, 267 (2019).
38. H. H. Heimes, C. Offermanns, A. Mohsseni, H. Laufen, U. Westerhoff, L. Hoffmann, P. Niehoff, M. Kurrat, M. Winter, and A. Kampker, "The effects of mechanical and thermal loads during lithium-ion pouch cell formation and their impacts on process time." *Energy Technology*, **8**, 1900118 (2020).
39. L. I. Rubio, M. J. Lain, and E. Kendrick, "Optimisation of formation and conditioning protocols for lithium-ion electric vehicle batteries." *Batteries & Supercaps*, **3**, 900 (2020).
40. F. J. Günter, C. Burgstaller, F. Konwitschny, and G. Reinhart, "Influence of the electrolyte quantity on lithium-ion cells." *J. Electrochem. Soc.*, **166**, A1709 (2019).
41. Dahn, "Physical review." *Physical review. B, Condensed matter*, **44**, 9170 (1991).
42. D. Allart, M. Montaru, and H. Gualous, "Model of Lithium Intercalation into Graphite by Potentiometric Analysis with Equilibrium and Entropy Change Curves of Graphite Electrode." *J. Electrochem. Soc.*, **165**, A380 (2018).
43. N. Nitta, F. Wu, J. T. Lee, and G. Yushin, "Li-ion battery materials: present and future." *Mater. Today*, **18**, 252 (2015).
44. I. Bloom, L. K. Walker, J. K. Basco, D. P. Abraham, J. P. Christophersen, and C. D. Ho, "Differential voltage analyses of high-power lithium-ion cells." *Journal of Power Sources*, **195**, 877 (2010).
45. X. Wu, K. Song, X. Zhang, N. Hu, L. Li, W. Li, L. Zhang, and H. Zhang, "Safety Issues in Lithium Ion Batteries: Materials and Cell Design." *Frontiers in Energy Research*, **7**, 65 (2019).
46. Y. Abe and S. Kumagai, "Effect of negative/positive capacity ratio on the rate and cycling performances of LiFePO4/graphite lithium-ion batteries." *Journal of Energy Storage*, **19**, 96 (2018).
47. F. J. Günter, J. Keilhofer, C. Rauch, S. Rössler, M. Schulz, W. Braunwarth, R. Gilles, R. Daub, and G. Reinhart, "Influence of pressure and temperature on the electrolyte filling of lithium-ion cells: Experiment, model and method." *Journal of Power Sources*, **517**, 230668 (2022).
48. N. Legrand, B. Knosp, P. Desprez, F. Lapicque, and S. Raël, "Physical characterization of the charging process of a Li-ion battery and prediction of Li plating by electrochemical modelling." *Journal of Power Sources*, **245**, 208 (2014).